OCEANOLOGIA

ORIGINAL RESEARCH ARTICLE

Imprints of atmospheric waves on the Black Sea surface in data of ocean color scanners

Marina A. Evdoshenko*

P.P. Shirshov Institute of Oceanology, Russian Academy of Sciences, Moscow, Russia

Summary Data from MERIS onboard Envisat and MODIS onboard Terra and Aqua for 15—16 May 2010 were used to study powerful imprints of atmospheric gravity waves (AGWs) on the western part the Black Sea surface. Two cold fronts crossed the sea following the warm front and caused the AGWs which modulated the sea surface. Imprints of AGWs appeared as stripes of alternating brightness, they had crest length more than a hundred kilometers and wavelength of units of kilometers. Wave amplitude of AGWs imprints, evaluated by a 90%-depth of light penetration into the sea at 490 nm z_{90}, the value inverse to the diffuse attenuation coefficient Kd_490, was units of decimeterxs. MODIS 250-m data of remote sensing reflectance, wind components and atmospheric pressure near the sea surface were obtained by processing the top of atmosphere data with the SeaDAS software package. Negative correlations of fluctuations of z_{90} with fluctuations of wind stress and atmospheric pressure were found on the transects of more than ten kilometers. The impact of wind stress on the origination of AGW imprints was found to be determinant, while the impact of atmospheric pressure was not more than units of percent.

* Corresponding author at: P.P. Shirshov Institute of Oceanology, Russian Academy of Sciences, 36 Nakhimovski prospect, 117997 Moscow, Russia.
E-mail address: maarsio@bk.ru

1. Introduction

Investigations of the footprints of atmospheric phenomena on the sea surface are traditionally carried out with the help of satellites equipped with devices termed synthetic aperture radar (SAR) systems. The microwave radiation of SAR freely penetrates through clouds into the sea to a distance of about several millimeters (Knyazev et al., 2003; Valenzuela, 1978). Atmospheric gravity waves (AGWs) which are generated in the marine planetary boundary layer (PBL), backscatter from the sea surface roughness and create a

periodic signal that is perceived by the radar (Alpers et al., 2008). AGWs are known to be generated by atmospheric fronts, horizontal or vertical wind shear or by airflow over mountain ranges, in which case they are called atmospheric lee waves. Imprints of AGWs with SAR devices installed onboard different satellites have been studied for several decades (Alpers and Brummer, 1994; Cheng and Alpers, 2010; Li et al., 2011; Vachon et al., 1994; Zheng et al., 1998).

AGWs are usually invisible but become visible at sufficiently high humidity appearing as "cloud streets" on top-of-the-atmosphere (TOA) reflectance images obtained from ocean color scanners. TOA data enable detailed investigations of cloud manifestations of atmospheric waves in the PBL (Da Silva and Magalhaes, 2009; Li et al., 2008; Liu et al., 2004).

Optical and near-infra-red radiance does not penetrate clouds, however, under a clear sky, ocean color scanners perceive the changing reflectance of the sea surface which AGWs modulate. Images from Envisat-ASAR and near-infrared images from MODIS-Terra revealed AGWs in different ocean regions (Li at al., 2011; Magalhaes et al., 2011). In (Evdoshenko, 2016) it was shown that the superimposition in a difference mode of MODIS TOA level 1 radiance image with signatures of AGWs in cloud, and remote sensing reflectance (Rrs) image of level 2 with signatures of AGWs on the sea surface, both at 859 nm, revealed that crests of the surface AGW imprints were similar the prolongations of AGW cloud stripes. Similar results were shown to be valid for different ocean regions. Numerical simulations and water tank experiments described by Sachsperger et al. (2017) showed that the vertical amplitudes of atmospheric gravity lee waves with wavelengths ~2-6 km depend on the inversion strength on the vertical temperature profiles measured in the PBL and can reach 300 m in size.

In the present paper, the numerous highly expressed long imprints of AGWs revealed by ocean color data on 15—16 May of 2010 which covered the western part of the Black Sea are analyzed. Such powerful AGW imprints in the Black Sea were found only once for the time period from the beginning of measurements with the ocean color scanner Sea-WiFS in 1998 and MODIS in 2002, until 2015. Evidently, they were connected with the very specific weather conditions produced during the passing of the warm and cold fronts over the sea. As a result, the intense AGWs were created in PBL; they spread down to the sea surface and modulated it. Vertical amplitudes of AGW imprints are evaluated and dependencies of the amplitudes from the atmospheric pressure and wind stress above the sea surface are stated.

The included ocean color satellite data, methods of their processing and data presentation are listed in section 2. Characteristics of AGW imprints and correlations of their amplitudes with some atmospheric characteristics are reflected in section 3. The main results obtained on the basis of the used satellite data are stated in section 4.

2. Material and methods

Data were obtained from three ocean color scanners: a medium resolution imaging spectrometer (MERIS) onboard Envisat and moderate resolution imaging spectroradiometers (MODISes) onboard EOS AM-1 Terra and EOS AM-2 Aqua satellites. We used the following data for 16 May 2010: MERIS full resolution (300-m) data M2010136084011.L2_FRS_OC, 1-km data of MODIS-Terra T2010136092000.L2_LAC_OC, MODIS-Aqua 250-m data A2010136110000.L1A_LAC and 1-km of MODIS-Aqua data A2010136110000.L2_LAC_OC. All these data are available at http://oceancolor.gsfc.nasa.gov. True-color level 1 TOA images from MODIS-Terra and -Aqua at 250-m resolution with no projection for 15—16 May 2010 are accessible at https://earthdata.nasa.gov/earth-observation-data.

Rrs at 859 nm originates in the thin topmost layer of about several centimeters owing to high absorption of pure water (Hale and Querry, 1973; Pegau et al., 1997), so it provides good reproduction of the imprints of atmospheric waves in water. Ocean color data of level 2: 250-m Rrs_859 and some atmospheric (meteorological) characteristics were generated from level 1 data with the SeaDAS software package. The process included several generation steps: 1 — the geolocation file, 2 — calibrated geolocated level 1b file and 3 — level 2 data. Meteorological data were initially obtained from the National Centers for Environmental Prediction (NCEP) and then processed with SeaDAS as level 2 products, namely: wind components at a height of 10 m above the ocean and atmospheric pressure near the sea surface; these data were automatically interpolated for a given time and place with the ocean color data. The SMCS software package (Sheberstov and Lukyanova, 2007) was used to plot the geographical maps of the obtained characteristics in the Mercator projection.

3. Results

We considered unusually long and intensive atmospheric waves and their imprints on the sea surface manifested over the Black Sea for two days. The Black Sea is a tideless marginal sea of the Atlantic Ocean that is divided into two sub-basins by a convexity extending south from the Crimean Peninsula. The maximum depth of 2212 m occurs in the center of the sea and the largest shelf is to the north of the basin which extends up to 190 km.

A map of the Black Sea with bathymetric contours of 50, 100, 500, 1000, and 2000 m is shown in Fig. 1. A polygon where imprints of AGWs were clearly manifested on all scanners images on 16 May 2010 is denoted by a black rectangle. A black circle designated the meteo-station Samsun, Turkey, on the southern shore of the sea where the radiosonde measurements were performed on those days.

On 15 May 2010 intensive atmospheric waves manifested as cloud structures of different forms over the entire Black Sea. The cloud patterns reflected atmospheric waves, convective cells and undular bores. Desaturated true-color TOA images of the sea with no projection at 250-m resolution from Terra-MODIS at 8:35 and from Aqua-MODIS at 10:20 2010 are shown in Fig. 2a and b. True-color images combine three spectral bands: band 1 (620—670 nm), band 3 (459—479 nm) and band 4 (545—565 nm). Fig. 2 shows that the western part of the sea was covered with fog and that against this background numerous AGWs signatures were observed as thick, near-linear cloud formations in the form
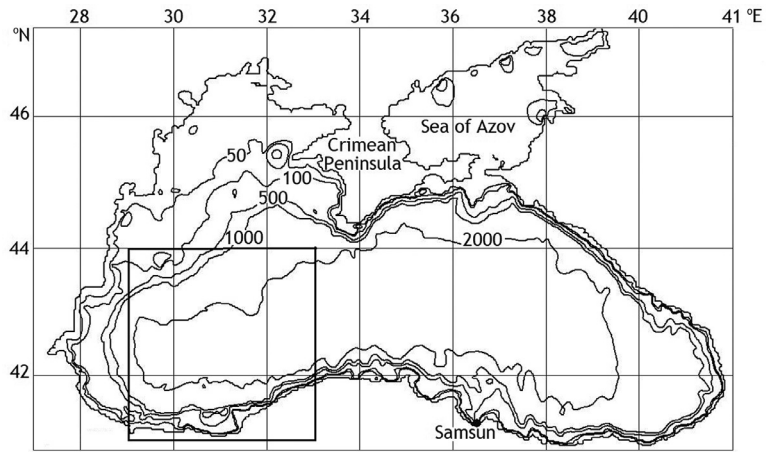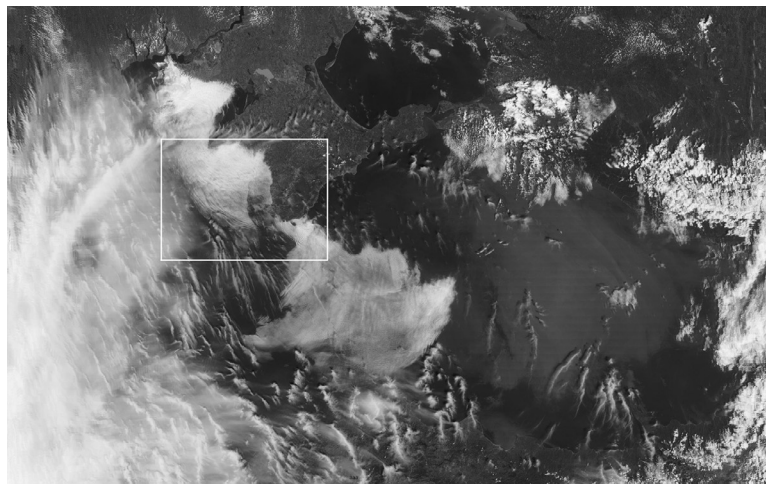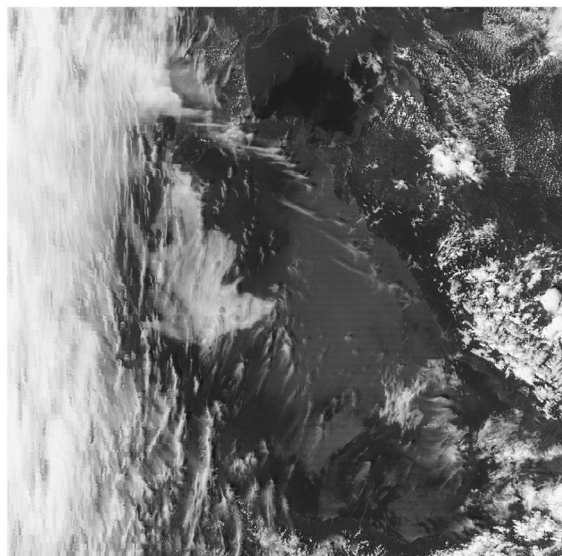
Figure 1   Map of the Black Sea with bathymetric contours Figure 8.

a

b

Figure 2   Desaturated true-color 250-m images of the Black Sea from: a — Terra-MODIS at 8:35, and b — Aqua-MODIS at 9:20 on 15 May 2010. The white square restricts an area with undular bores.
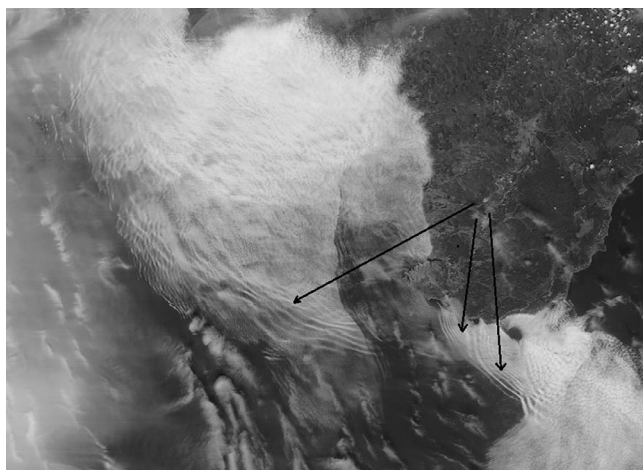
Figure 3 Desaturated true-color 250-m image of a series of undular bores (indicated by black arrows) to the south of the Crimean Peninsula obtained from Terra-MODIS at 8:35 on 15 May 2010.

of separate cloud streets in the north-eastern part of the sea.

The northern central part of the Black Sea, which contains undular bore clouds (is bound by a white square in Fig. 2a) is scaled up in Fig. 3. A series of low-level clouds in the form of narrow, arched stripes of atmospheric wave manifestation (indicated by black arrows in Fig. 3) is clearly seen propagating toward the southern Crimean Peninsula; undular bore clouds were imposed on each other. It is known that a thunderstorm may assist with the occurrence of undular bores and that undular bores can, in turn, intensify a thunderstorm because they further disturb the atmosphere (Chanson, 2010). Seemingly, there was a thunderstorm or hurricane on 15 May 2010.

On the following day, 16 May 2010, the cloudiness dispersed above almost the entire Black sea. Three ocean color sensors — MERIS at 8:40, Terra-MODIS at 9:20 and Aqua-MODIS at 11:00 — recorded unusual surface imprints of AGWs in the Black Sea on that day only. Apparently, imprints of

AGWs on the sea surface existed for two days — on 15 and 16 May 2010, but a strong fog on 15 May prevented their observation with ocean color scanners, as the light in the visible range does not penetrate through strong fog or haze. A picture showing clear AGW signatures in the Black Sea on 16 May 2010 was unique for the period from 1998 until 2015.

The desaturated true-color TOA images of the western part of the Black Sea at 250-m resolution obtained on 16 May 2010 from Terra-MODIS at 9:20 and Aqua-MODIS at 11:00 are shown in Fig. 4a and b. These figures show practically the same western part of the Black Sea but have different sizes because they are represented without any projection and with no latitude-longitude axes (available at https://earthdata.nasa.gov/earth-observation-data). On both images numerous AGWs of different directions are seen on the background of sun glitter. They most clearly appeared in the left western part of the sea. Imprints of AGWs in the form of long waves are evident; they represented AGWs because they were very long, narrow and close to rectilinear; a width of their crests expressed as light stripes was significantly less than the width of troughs expressed as dark stripes. These characteristics differentiate AGWs from the signatures of internal surface waves, according to Alpers and Huang (2011). The wave pattern very likely originates from AGWs if a sea area has no shallow underwater bottom topography, no strong tidal currents, and no upwelling — conditions satisfied by the Black Sea. Most of the manifested waves were oriented SW—NE, while others were oriented in different directions. Imprints of AGWs are observed to intersect each other. These phenomena could be caused by the imposition of traces of AGWs propagating at different levels of the marine PBL.

Similar surface imprints were also apparent at a pattern of *Rrs* at wavelengths of the optical and near-infrared ranges. They were also visible on images of standard ocean color products, as the diffuse attenuation coefficient of sunlight in the sea — Kd_490, and other products (accessible at http://oceancolor.gsfc.nasa.gov).

The empirical algorithm for an indicator of the turbidity of the water column in the transparency window Kd_490, in m^{-1}, returns the diffuse attenuation coefficient for downwelling irradiance at 490 nm, calculated using a
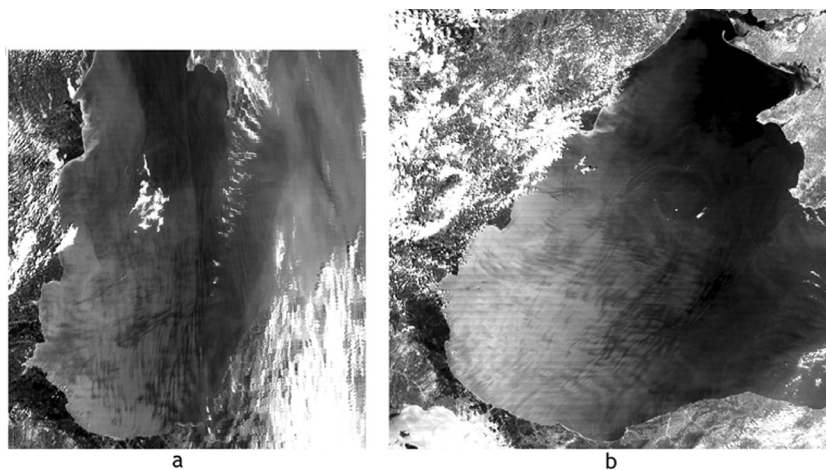

a				b

Figure 4 Desaturated true-color 250-m TOA images of the western part of the Black Sea on 16 May 2010: a — at 9:20 from Terra-MODIS, and b — at 11:00 from Aqua-MODIS.
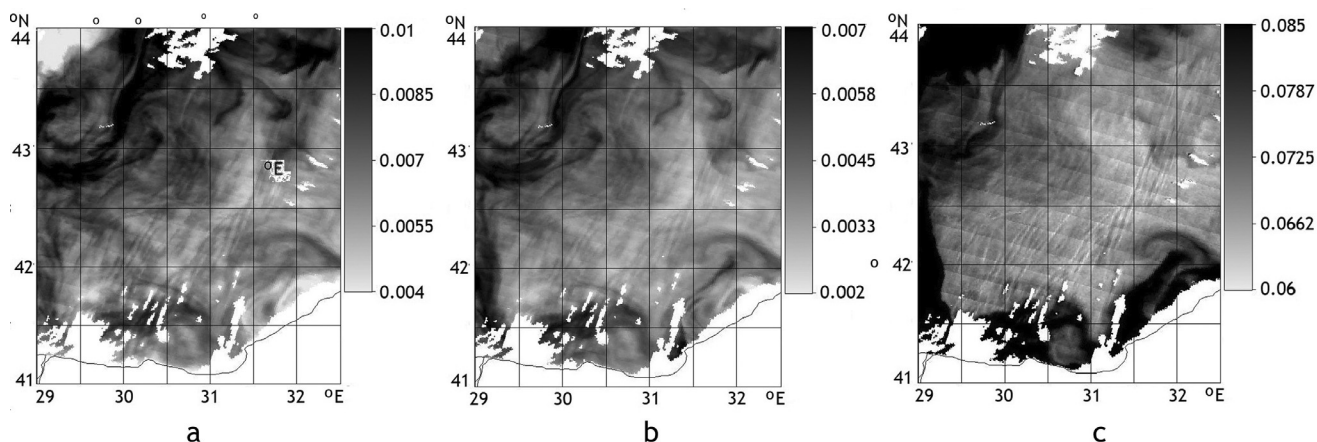
Figure 5 Images obtained from Terra-MODIS on 16 May at 9:20 of the testing area restricted by a black rectangle in Fig. 1: a — Rrs_488, sr^{-1}; b — Rrs_547, sr^{-1}; c — Kd_490, m^{-1}.

relationship derived from in situ measurements of Kd_490 and the blue-to-green band ratios of Rrs (Lee et al., 2005, Morel et al., 2007). Kd_490 over the first optical attenuation layer is calculated based on the following fourth-order polynomial relationship:

$$\log_{10}(K_{bio}\_490) = a_0 + \sum_{(i=1)}^{4} a_i \left(\log_{10}(Rrs\_\lambda_{blue}/Rrs\_\lambda_{green})\right)l,$$

$$Kd\_490 = K_{bio}\_490 + 0.0166. \qquad (1)$$

For MODIS, $\lambda_{blue} = 488$ nm and $\lambda_{green} = 547$ nm; for MERIS, $\lambda_{blue} = 490$ nm and $\lambda_{green} = 560$ nm; the coefficients a_0, a_1, a_2 a_3, and a_4 are also sensor-specific (https://oceancolor.gsfc.nasa.gov/atbd/kd_490).

Suslin et al. (2017) showed that for the clear waters ($Kd\_490 \leq 0.07$) of the western Black Sea, MODIS Kd_490 data calculated for different seasons differed weakly with sea measurements made with an immersible Bulgarian buoy **basbio001d**. For the more turbid waters ($Kd\_490 \geq 0.12$) of the western Black Sea, the discrepancy with sea measurements was minimal in the warm season — from the second half of May to the end of September, whereas for the cold period of a year, the standard satellite values of Kd_490 were reduced by approximately ∼20%. Thus, on 16 May, the standard values of Kd_490 were close to the real ones even for more turbid waters with $Kd\_490 \geq 0.12$.

Kd_490 in the Black Sea originates at a depth of 10—20 m (Karabashev et al., 2007), so factors such as eddies, fronts and increased concentrations of phytoplankton may play a dominant role and mask possible traces of AGWs in the surface layer. In deep-sea regions, where the amount of phytoplankton is significantly less, the signatures of AGWs on the sea surface can be quite noticeable.

Images of Rrs_488, Rrs_547, and Kd_490 from Terra-MODIS obtained on 16 May at 9:20 for the deep central south-west part of the sea, enclosed in the black rectangle in Fig. 1, are shown in Fig. 5a,b and c. Values of Kd_490 in Fig. 5c did not exceed 0.09, so sea waters in the considered region were clean. Thus values of the standard NASA product Kd_490 calculated by the relationship (1) is valid for the considered time of the year and south-west region of the Black Sea. On all three images, the traces of AGWs as

narrow stripes elongated in a SW—NE direction are clearly observed in the testing area; best of all, they appeared on the image of Kd_490 (Fig. 5c). Lee et al. (2005) points out that Kd_490 depends not only on optical properties of the water (hydrosol, pigments, dissolved matter etcetera), but also varies to some extent with surface conditions.

The diagonal strips manifested on the Kd_490 image (Fig. 5c) are caused by an imperfect relative correction between the along-track detectors of the scanner MODIS, apprehending the upcoming radiation (Frantz, 2006).

We evaluated a vertical scale of AGW imprints in the sea surface or amplitudes of surface waves induced by AGWs. For this aim we used an approximate relation between Kd and a penetration depth of light in the sea corresponding to the first irradiance attenuation length z_{90}. Gordon and McCluney (1975) defined the value z_{90} as the depth above which 90% of the diffusely reflected irradiance (excluding specular reflectance) originates:

$$z_{90} \approx 1/Kd. \qquad (2)$$

Values of z_{90} have a dimension of meter. For the clear deep water of the Black Sea, it is acceptable to consider that fluctuations of the light penetration depth in the sea correspond and equal to fluctuations of the sea level under the impact of AGWs. This allows the ability to estimate vertical amplitudes of AGWs in the sea by the fluctuations of z_{90}. Using Eq. (2), we calculated approximate values z_{90} at 490 nm from data of Kd_490. The presented method of evaluation of z_{90} at 490 nm by data of Kd_490 in the northeastern part of the Black Sea surface obtained from MODIS-Terra and -Aqua on 21 April 2007 was used earlier in (Evdoshenko, 2014).

Calculations were made for three ocean color scanner data for 16 May 2010: MERIS at 8:40, Terra-MODIS at 9:20 and Aqua-MODIS at 11:00. Images of z_{90} from the scanners for the rectangular region shown in Fig. 1 are presented in Fig. 6a,b, and c. Signatures of AGWs on the images of z_{90} were noticeable on the background of the underlying eddies and mushroom-like structures. Transects **A**, **B**, and **C** across clear imprints of AGWs were made for the regions, which were mostly free of sea eddies. This made it possible to minimize errors in the depth of light penetration into the
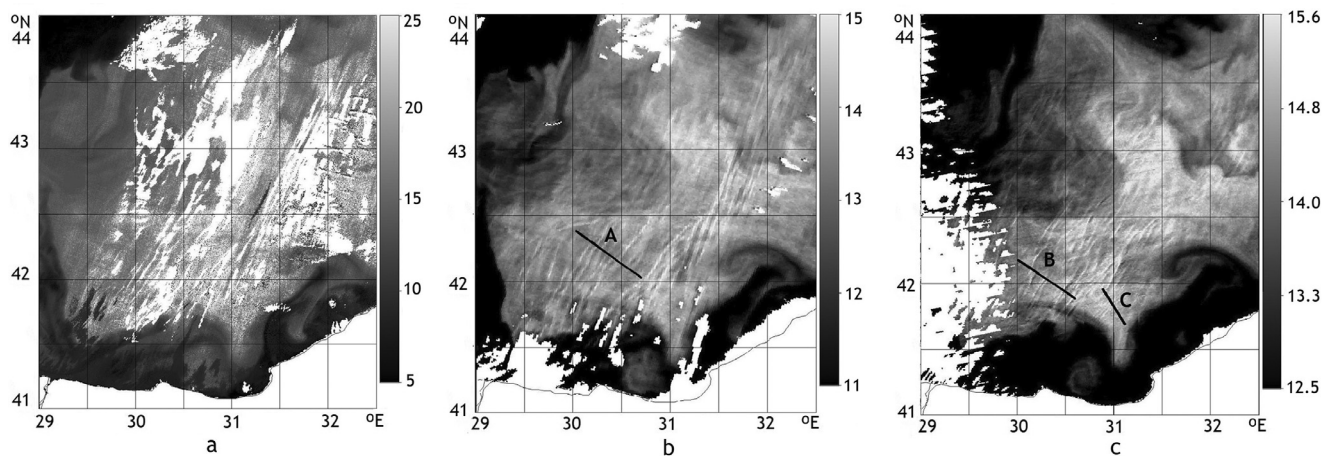
Figure 6 Images of z_{90} of the western part of the Black Sea from: a — MERIS at 8:40; b — Terra-MODIS at 9:20; c — Aqua-MODIS at 11:00; all on 16 May 2010. Transects across imprints of atmospheric waves are shown by black lines; transect **A**: 42.301°N, 30.102°E—42.170°N, 30.458°E; transect **B**: 42.036°N, 30.032°E—41.897°N, 30.273°E; transect **C**: 41.880°N, 30.951°E—41.787°N, 31.030°E.
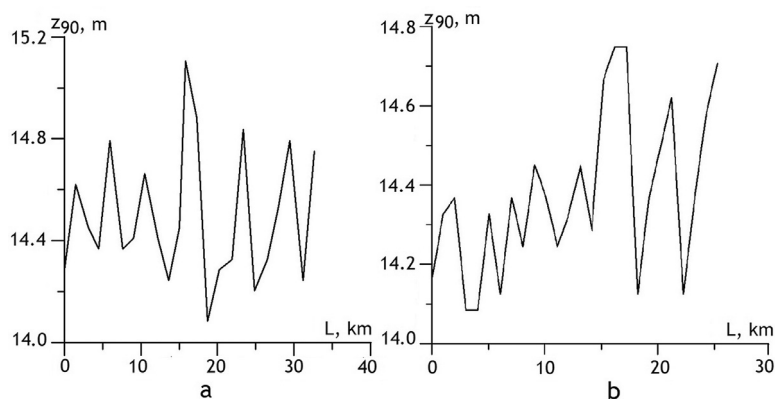

Figure 7 Distributions of $z_{90}(L)$ across AGW imprints at 11:00 on 16 May 2010 (see Fig. 6b and c): a — at the transect **A**; b — at the transect **B**.

sea connected with other mesoscale structures that were distinct from AGWs. Transects are indicated by black lines.

The AGW pattern appeared in z_{90} images in the deep sea at depths greater than 1 km. Towards 8:40, cloudiness was intermittent, so imprints of atmospheric waves alternated with cloudy manifestations. Fig. 6b, and c show that AGWs effectively modulated the sea surface to cause changes in the sunlight penetration depth. The main direction of the imprints are SW—NE, but several signatures of AGWs in directions NW—SE are also noticeable in Fig. 6b; these multidirectional imprints are superimposed on each other. Comparison of the patterns of AGW signatures on the images of z_{90} shown in Fig. 6b, and c allows us to conclude that, from 9:20 to 11:00, the wavelength and crest length of the imprints became smaller, but the number of imprinted waves increased; that is, the AGWs began to break up into smaller ones. The length of the wave imprints exceeded 150 km in some cases.

Plots of the surface wave at the transects $z_{90}(L)$ **A** and **B**, where L is distance, for 9:20 and 11:00 on 16 May 2010, are shown in Fig. 7a, and b. Fig. 7a shows that the imprints of AGWs at the transect **A** at 9:20 had a wavelength of more than 5 km, while at the transect **B** at 11:00, the mean wavelength was 3.3 km. We evaluated a modulation depth, or a

vertical scale of imprinted waves at the transects, using the plots of z_{90} for dimensional considerations. A value of $z_{90\,max}$ corresponds to a wave crest, while the value of $z_{90\,min}$ corresponds to the wave trough; a discrepancy Δz_{90} between $z_{90\,max}$ and $z_{90\,min}$ corresponds to the wave height. The wave amplitude, as a half of the wave height, was 10—50 cm at the transect **A**, and 5—33 cm at the transect **B**. Thus, during the 100 min period between the Terra and Aqua flights, the surface wave amplitude and wavelength decreased; that is, the AGWs became weaker.

Fig. 8 shows the image of the 250-m *Rrs*_859 from Aqua-MODIS at 11:00 for the western part of the Black Sea. Traces of atmospheric waves of different forms and wavelengths are seen in the deep sea, as well as in the coastal regions, as *Rrs*_859 reflects phenomena in the upper layer of several centimeters. Signatures of smaller AGWs of different forms and directions are seen. Imprints of AGWs with a SW—NE direction are intersected by imprints of AGWs directed approximately W—E which evidently spread at a higher altitude. Near 44°N, 30°E, a circular structure is observable, caused possibly by an atmospheric eddy with a diameter of about 100 km which modulated the AGW packet.

Wind speed and direction at a height of 10 m and air pressure near the sea surface for the western part of the
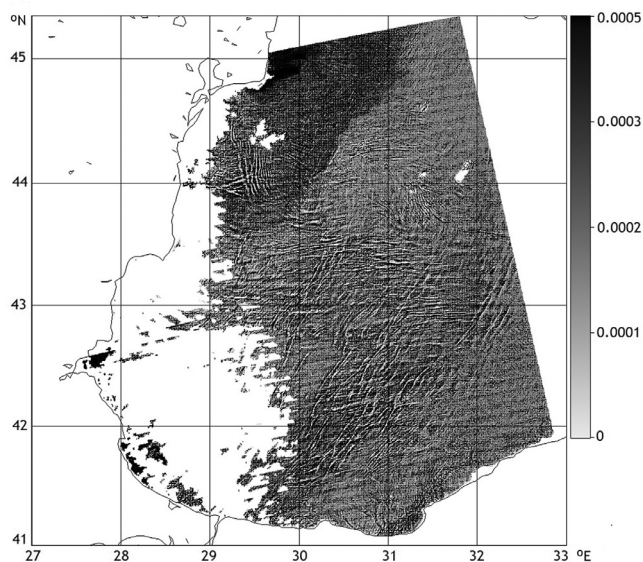
Figure 8 Image of 250-m $Rrs(859)$, sr^{-1} from Aqua-MODIS at 11:00 on 16 May 2010.

Figure 10 Depth of light penetration into the sea z_{90} (solid line) and air pressure near the sea surface P (dotted line) depending on the distance L at the transect which passes approximately along the isobar $P = 1006$ mb at 11:00 on 16 May 2010.

Black Sea at 11:00 on 16 May 2010 were calculated, they are shown in Fig. 9a, and b respectively. Wind generally blew from the south-west and reached 10 ms^{-1} in the middle of the western part of the sea, decreasing to 5—8 ms^{-1} near the shore. A comparison of Fig. 9a and Fig. 6a, b, and c suggests that the AGW signatures were oriented mainly downwind: i.e. SW—NE. The air pressure increased almost monotonically in the NW—SE direction from 1000.5 to 1006.5 mb, as seen in Fig. 8b. Transects along the 9 ms^{-1} isotach and along the isobar of 1006 mb which cross clear imprints of AGWs, are shown by thick black lines in Fig. 9a and b, respectively.

Atmospheric forcing could be expressed by way of pressure and wind stress on the sea surface (Rabinovich, 2008). For confirmation of the interrelationship between signatures of long surface waves and the atmospheric impact, we compared the fluctuations z_{90}, air pressure P above the sea surface, wind speed U, and wind stress τ. For this purpose we chose transects that crossed the sea surface imprints and passed approximately along the isolines of the atmospheric
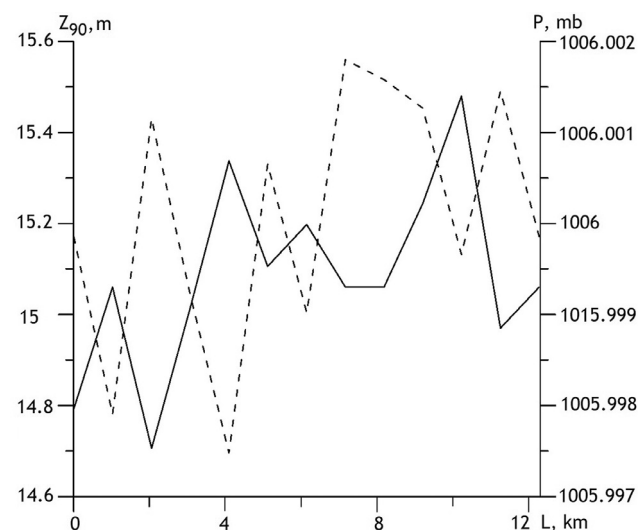
characteristics; it was done with the aim to eliminate low-frequency atmospheric trends in the best way.

A 12-km transect **C** (41.880°N, 30.951°E—41.787°N, 31.030°E) that intersected the z_{90} signatures at 11:00 on 16 May 2010 (see Fig. 6c) was chosen along the isobar of 1006 mb; it is also shown in Fig. 9b. The transect crosses the AGW imprints at an angle of approximately 25° normal of them. The distributions of z_{90} and P at the transect are shown in Fig. 10. The vertical amplitude of AGW imprints was 15—33 cm; a negative cross-correlation was evident between z_{90} and P.

Before calculating a cross-correlation between the modulation depth and atmospheric pressure, the polynomial low pass trends of the second order were removed from the z_{90} and P series. The resulting cross-correlation was −0.63. Note, however, that the data used were obtained in various ways: z_{90} or Kd_490 — from MODIS data with resolution of 1 km, and surface pressure P — from meteo-observations combined with data from meteorological satellites, with a general resolution of 5 km. The obtained negative cross-
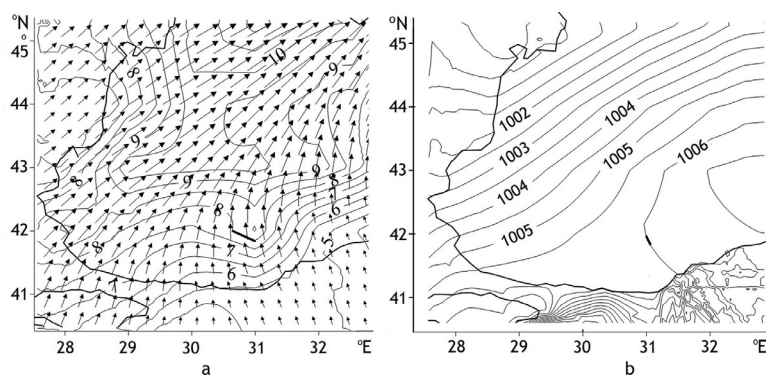

Figure 9 a — wind speed in ms^{-1} (isolines) and direction (arrows) at 10 m above the surface, b — air pressure in mb near the surface for the western Black Sea at 11:00 on 16 May 2010.
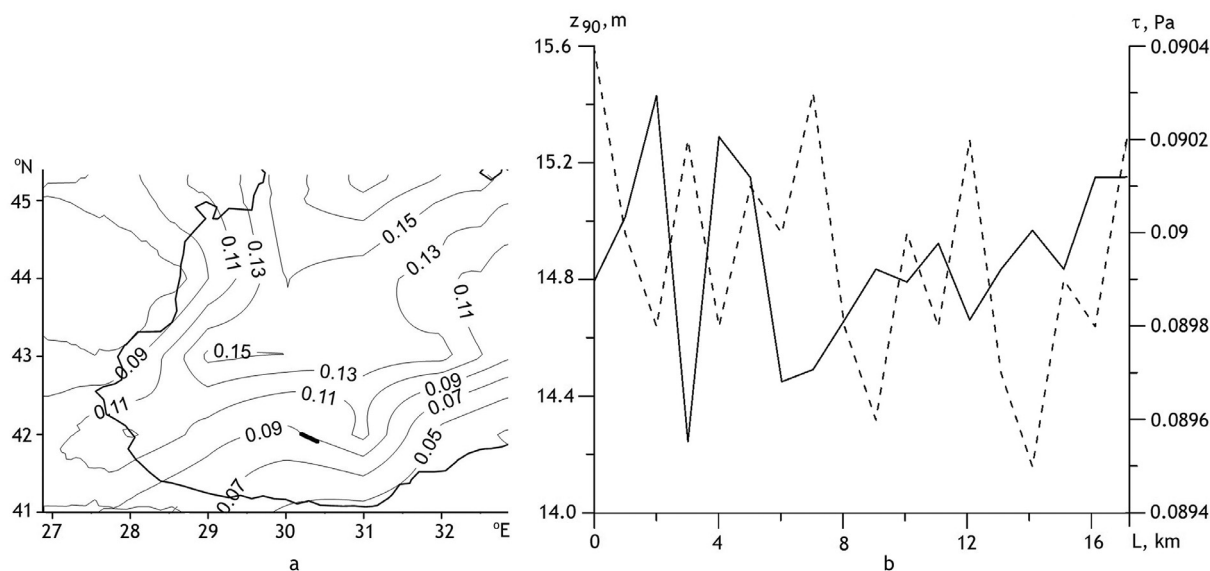
Figure 11 a — isolines of wind stress τ at the height of 10 m, transect passing approximately along the part of the isoline $U = 0.09$ Pa is shown by a thick line; b — depth of light penetration into the sea z_{90} (solid line) and wind stress τ at 10 m above the sea surface (dotted line) depending on the distance L at the transect at 11:00 on 16 May 2010.

correlation would be much more of an absolute value if errors connected with inconsistency caused by the different acquisition methods were also taken into account.

It is known that the inverted-barometer response to air pressure forcing fulfills the condition whereby an atmospheric pressure of 1 mb causes a negative response in the sea level of 1 cm (Wunsch and Stammer, 1997). It is seen from Fig. 10 that the relations of pairs of anticorrelated amplitudes of A(z_{90})/A(P) greatly exceed the inverted-barometer response. Similar cases of the exceeding of the inverted-barometer relation was noted long ago. For example, Donn and McGuiness (1960) recorded a continuous and simultaneous series of oceanic oscillations of sea water level measured by a tsunami detector and oscillations of atmospheric pressure measured by a microbarovariograph with a period of 4—10 min, recorded on 20 September 1958 on the continental shelf southeast of New York at the forth Texas Tower. Air-pressure oscillations of 0.05 mb caused sea-level oscillations of 1.5—4 cm, with a magnification of 80—115 times relative to the inverted barometer. At the time of the measurements, a cold front had passed above the region, causing an inversion of the vertical profile of the air temperature. In the Mediterranean Sea, planetary atmospheric waves caused sea level overshoots far above the inverted-barometer response at subinertial frequencies (Malacic and Orlic, 1993). The authors implied that the Mediterranean Sea level was forced not only by the air pressure, but also by some other agent — most probably wind.

An interrelation between the fluctuations of z_{90} and wind speed U was also examined in the western part of the Black Sea. For this purpose a transect was chosen along the isotach of $U = 8$ ms^{-1} (41.85°N, 31.00°E—42.00°N, 30.64°E) across AGW signa tures (Fig. 9a). No correlation was discovered between the fluctuations of z_{90} and of U.

Another characteristic of atmospheric forcing that roughens the sea surface and creates imprints of AGWs could be wind stress. Wind stress is important in air-sea interactions

and forced oceanic variability and is calculated by the following empirical formula (Fairall et al., 2003):

$$\tau = C_d \rho_a U^2, \tag{3}$$

where ρ_a is the air density (about 1.22 kg m^{-3}), and C_d is a dimensionless drag coefficient with a typical value of 0.0013. Wind stress is a square function of wind speed because the wind force depends on the wind speed and sea roughness, which in turn depends on wind speed (Kochanski et al., 2006). Wind stress was calculated using the Eq. (3); a map of τ-isolines is plotted in Fig. 11a, which shows that τ changed from 0.05 to more than 0.17 Pa in the western part of the sea. A transect along $\tau = 0.09$ Pa (42°N, 30.214°E—41.933°N, 30.402°E) is plotted to cross clear imprints of AGWs in the south-western part of the sea. Distributions of z_{90} and τ at the transect are shown in Fig. 11b.

A clear negative correlation is evident between z_{90} and τ at the transect. Before the calculation of a cross correlation, a filtration with low-pass filters in the form of polynomials of the second order was conducted on the compared series; the resulting cross correlation equals −0.53. The obtained negative cross-correlation would have a much greater absolute value if the errors connected with the inconsistency of the series of U and z_{90} and amplification by U-squaring were taken into account.

Wind stress τ and atmospheric pressure above the sea surface P can be measured in the same units of pressure — pascal, as 1 mb = 0.01 Pa. We now compare the relationships of the pairs of negatively correlated amplitudes of values measured at the transects which are shown in Fig. 10 and Fig. 11b. Evaluations revealed a mean relation A(P)/A(z_{90}) = 6e^{-5} Pa m^{-1} at the transect shown in Fig. 10, and a mean relation A(τ)/A(z_{90}) = 2e^{-3} Pa m^{-1} at the transect shown in Fig. 11b. Comparing the mean values A(P)/A(z_{90}) and A(τ)/A(z_{90}) allows the conclusion that the impact of the wind stress on amplitudes of the imprints exceeded that of atmospheric pressure by about 33 times.
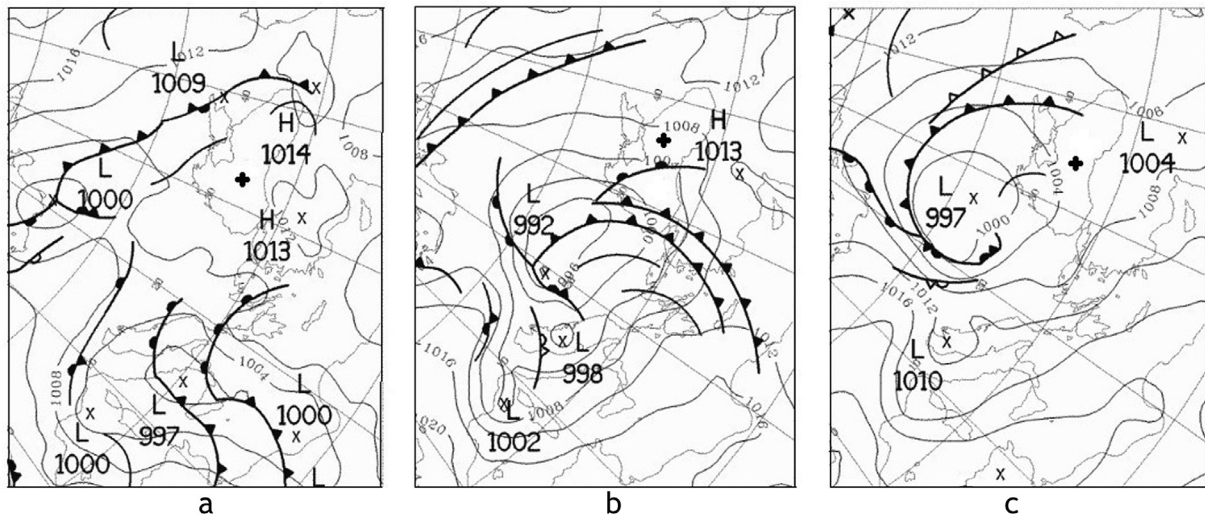
Figure 12 Weather maps for Europe at 00:00 UTC on: a — 15 May, b — 16 May, c — 17 May 2010; the Black Sea is indicated with a four-pointed star.

That is, the contribution of wind stress to induced surface waves was predominant, whereas the contribution of atmospheric pressure was only about 3%. The latter circumstance can explain the multiple times the inverted-barometer response appeared at the transect depicted in Fig. 10b, since the main impact on the sea surface caused by AGWs was due to wind stress rather than atmospheric pressure.

Surface weather maps for the Europian region at 00:00 on three successive days: 15, 16 and 17 May 2010 (available at http://metoffice.gov.uk) are shown in Fig. 12a,b, and c (the Black Sea is designated by a four-pointed star). On 15—16 May, a high-pressure area of 1014 mbar was located over the Black Sea, and a low-pressure core of 997 mbar occurred over the Mediterranean Sea near Italy. This pressure distribution is evidence of the existence of atmospheric fronts over the Black Sea. In actuality, the weather map for 16 May shows that a warm front was moving from the south across the Black Sea and that two cold fronts from the west had begun to cross the sea, in accordance with the wind direction shown in Fig. 9a. The angle between the isobars above the sea (Fig. 12b) was nearly normal, indicating that the fronts were moving quickly. Sea regions, which are visible in Fig. 2, were evidently covered by pre-frontal or warm-frontal fog, which often occurs over large regions ahead of warm fronts. The atmospheric waves in the form of strong cloud streets are known to originate in the vicinity of fronts (Plougonven and Zhang, 2014). Fig. 12c shows that the air pressure dropped over the Black Sea on 17 May, and cold fronts turned and formed a cyclone in the north-west area of the sea.

The single available meteo-station located on the Black Sea shore, starting upper air radiosondes, was Samsun (Turkey) on the southern shore of eastern part of the sea (see Fig. 1). The values of the characteristics measured at the Samsun station at 12:00 UTC on 16 May 2010 of the low atmosphere were obtained from http://weather.uwyo.edu/upperair/sounding.html. A thermodynamic diagram (tephigram) and vertical distributions of wind speed and wind direction corresponding to those measurements are shown in Fig. 13. A prominent temperature
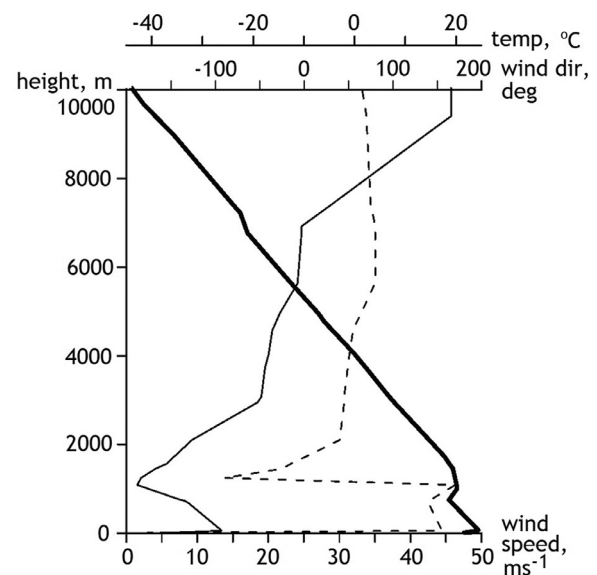

Figure 13 Measurements at the radiosonde station Samsun obtained at 12:00 UTC on 16 May 2010: vertical profiles of temperature (bold solid line), wind speed (solid line), and wind direction (dotted line).

inversion with a potential increase $\Delta\theta$ of 1.6°C, with the base at 746 m and the top at 1001 m, which is seen from Fig. 13, implies that the atmosphere was stably stratified. The inversion shows that the frontal zone represents a transition zone between two distinct air masses, separating the cold, dry air below the inversion from the warmer, moister air above it. Evidently, the cold front(s) crossed the sea and left a mark on the tephigram on 16 May in the form of a frontal inversion. The vertical extent of the frontal inversion was limited to the vertical extent of the frontal zone itself. Similar inversions on vertical profiles of wind direction centered at 1087 m and wind speed centered at 1087 m confirm the atmospheric stability in the layer at about 1 km. AGWs are well known can exist in a stably stratified atmosphere

(Nappo, 2002). An inversion on vertical profiles of low-level air temperature and wind can act like a waveguide and trap the AGWs (Cheng and Alpers, 2010). This is consistent with the situation considered here, where numerous imprints of atmospheric waves appeared on the sea surface. Air temperature and wind speed measured at the station Samsun on 16 May 2010 increased in the vertical layer from about 1000 m up the near water layer (about 60 m), and then decreased up to the sea surface providing significant vertical gradients. These gradients assisted AGWs in spreading downward and modulating the sea surface.

We suppose that the cold front had not yet reached the Samsun station on 15 May at 12:00, so it could not leave a mark on the tephigram that day. The data from Samsun show that the mean wind speed near the surface was 10 ms^{-1}, which is slightly more than the wind speed near the shore, calculated on the base of Aqua-MODIS data from 16 May 2010 at 11:00, but the divergence could be caused by the remoteness of the Samsun meteo-station from the western part of the sea. Comparison of the wind field maps, surface weather maps, and radiosonde data with sea surface imprints on 16 May 2010 leads us to conclude that the wave-like patterns are associated with atmospheric fronts; therefore we define the atmospheric waves as frontal waves (Liu, 2010).

Undular bores can be a result of collision of the warm and cold front, and the cold front moves through the stable atmosphere in the low levels (Coleman et al., 2010). Evidently a similar situation was observed on 15 May 2010 in the north-western part of the sea when several undular bores were spreading to the south-west from the Crimean Peninsula (Fig. 3). An additional reason for bore origination could be that a less expansive cold front passed over the peninsula extending southward from the low-pressure region.

The image of Rrs_859 (Fig. 8) shows the appearance of AGW imprints on 16 May 2010 on the entire western part of the sea from near the shore regions with depths less than 100 m to the deepest parts with depths about 2200 m (see Fig. 1), and imprints visible on images of z_{90} appeared in the limited region from about 29.30°N, 41.5°E—32.50°N, 43.5°E (Fig. 6), with depths H from 500 m to 2200 m. A phase speed of ocean surface waves C_{ow} is defined according to Phillips (1977):

$$C_{ow} = \sqrt{\frac{g\lambda}{2\pi}\tanh\left(2\frac{\pi H}{\lambda}\right)}, \qquad (4)$$

where λ is the wavelength of wavy imprints, H is the depth, and g is the acceleration due to gravity. The phase speed of C_{ow} for shallow waters with a depth H of 100 m was 31 m s^{-1}, while for deep sea regions it ranged from 68 to 88 m s^{-1}.

Based on the radiosonde data from the Samsun meteo-station, we can define the local atmosphere as a two-layer system with the interface at the inversion layer height of 1000 m (see Fig. 13). A phase speed of atmospheric waves c_0 could be defined by a vertical profile of air temperature below and above the positive inversion $c_0 = \sqrt{g'h_0}$, where g' is the reduced gravity acceleration, and h_0 is the characteristic depth of the waveguide (Magalhaes et al., 2011). The value of h_0 is calculated as $h_0 = d_m d_p/(d_m + d_p)$ where d_m

and d_p are the thicknesses of the lower and upper layers, respectively (Li et. al., 2004). We define $d_m = 1000$ m, and $d_p = 6000$ m, so that $h_0 = 857$ m. The reduced gravity acceleration $g' = 0.1$ m s^{-2}, so that $c_0 = 9.26$ m s^{-1}. As shown in Fig. 9a, c_0 practically coincided with the wind speed in the deep part of the sea.

Thus, as the calculations showed, the phase speed of atmospheric waves c_0 was considerably smaller than the speed of long sea waves C_{ow}, so that the Proudman resonance, when the condition of equal speeds of atmospheric and sea waves are equal (Monserrat et al., 2006), was not fulfilled. Therefore we conclude that sea surface imprints were not caused by a resonance interaction between atmospheric and sea waves, but were caused by instantaneous effect on the sea surface of unusually power atmospheric waves by way of wind stress and atmospheric pressure.

4. Conclusions

The satellite observations at the western Black Sea on 16 May 2016 by Envisat-MERIS, Terra-MODIS, and Aqua-MODIS revealed power imprints of atmospheric gravity waves on the sea surface. These imprints appeared clearly on remote sensing reflectance images of Rrs at different wavelengths, and most strongly on images of Rrs at 859 nm. They were also manifested on images of diffuse attenuation coefficient of light Kd_490, and therefore on images of the light penetration depth z_{90} at 490 nm. Wave imprint amplitudes evaluated for the dimensional consideration by values of z_{90} at transects that crossed imprints normal to them changed from less than 5 cm to more than 50 cm. The crests of the imprinted waves exceeded 150 km in length and the wavelength changed from less than 2 to more than 5 km. Distributions at the transect along the isobar P showed a significant negative correlation of fluctuations of z_{90} with P. Similarly, distributions at the transect along the isoline of the wind stress τ showed also a significant negative correlation of fluctuations z_{90} with τ. This statistical analysis confirms the atmospheric nature of the wavy imprints. The wind stress effect on amplitudes of the sea surface imprints was found to be about 30 times more intense than the effect of atmospheric pressure.

Two cold fronts crossed the Black Sea on 16 May 2010. The fronts caused inversions on vertical profiles of air temperature, wind speed, and wind direction at a height of about 1000 m, obtained from radiosonde measurements on the southern shore of the sea. The inversions created a stably stratified layer of atmosphere that could act like a waveguide, trapping the AGWs. Strong vertical stratification of temperature and wind speed from the height of the inversion up to the sea surface promoted the expansion of atmospheric waves downward and impacted the surface to cause imprints.

Acknowledgements

References

Alpers, W., Brummer, B., 1994. Atmospheric boundary layer rolls observed by the synthetic aperture radar aboard the ERS-1 satellite. J. Geophys. Res-Oceans. 99 (C6), 12613—12621, https://doi.org/10.1029/94JC00421.

Alpers, W., Huang, W., 2011. On the discrimination of radar signatures of atmospheric gravity waves and oceanic internal waves on synthetic aperture radar images of the sea surface. IEEE T. Geosci. Remote. 49 (3), 1114—1126, https://doi.org/10.1109/TGRS.2010.2072930.

Alpers, W., Huang, W., Xilin, G., 2008. Observations of atmospheric gravity waves over the Chinese seas by spaceborne synthetic aperture radar. Proc. Dragon (ESA SP-655, April 2008).

Chanson, H., 2010. Undular bores. In: Second International Conference on Coastal Zone Engineering and Management. November 1—3, 2010. Muscat, Oman, 12 pp.

Cheng, C.M., Alpers, W., 2010. Investigation of trapped atmospheric gravity waves over the South China Sea using Envisat synthetic aperture radar images. Int. J. Remote Sens. 31 (17—18), 4725—4742, https://doi.org/10.1080/01431161.2010.485145.

Coleman, T.A., Knupp, K., Herzmann, D.E., 2010. An Undular Bore and Gravity Waves Illustrated by Dramatic Time-Lapse Photography. J. Atmos. Ocean. Tech. 27 (8), 1355—1361, https://doi.org/10.1175/2010JTECHA1472.1.

Da Silva, J.C.B., Magalhaes, J.M., 2009. Satellite observations of large atmospheric gravity waves in the Mozambique Channel. Int. J. Remote Sens. 30 (5), 1161—1182, https://doi.org/10.1080/01431160802448943.

Donn, W.L., McGuinness, W.T., 1960. Air-coupled long waves in the ocean. J. Meteorol. 17, 515—521, https://doi.org/10.1175/1520-0469(1960)017⟨0515:ACLWIT⟩2.0.CO;2.

Evdoshenko, M.A., 2014. Meteorological Waves (by Ocean Color Scanner Data). Dokl. Earth Sci. 458 (2), 1241—1245, https://doi.org/10.1134/S1028334X14100043.

Evdoshenko, M.A., 2016. Detecting imprints of atmospheric waves in the Bering Sea with MODIS data. Oceanologia 58 (4), 264—271, https://doi.org/10.1016/j.oceano.2016.04.003.

Fairall, C.W., Bradley, E.F., Hare, J.E., Grachev, A.A., Edson, J.B., 2003. Bulk parameterization of air-sea fluxes: Updates and verification for the COARE algorithm. J. Climatol. 16 (4), 571—591, https://doi.org/10.1175/1520-0442(2003)016⟨0571:BPOASF⟩2.0.CO;2.

Franz, B.A., Werdell, P., Meister, G., Kwaitkowska, E.J., Bailey, S., Ahmad, Z., McClain, C.R., 2006. MODIS land bands for ocean remote sensing applications. Proc. P. Soc. Photo-Opt. Ins. XVIII. Montreal, Canada 9—13 October. https://www.researchgate.net/publication/234025610.

Gordon, H.R., McCluney, W.R., 1975. Estimation of the depth of sunlight penetration in the sea for remote sensing. Appl. Optics 14 (2), 413—416, https://doi.org/10.1364/AO.14.000413.

Hale, G.M., Querry, M.R., 1973. Optical constants of water in the 200-nm to 200-μm wavelength region. Appl. Optics 12 (3), 555—563, https://doi.org/10.1364/AO.12.000555.

Karabashev, G.S., Evdoshenko, M.A., Sheberstov, S.V., 2007. Correlation of distributions of normalized spectral radiances as an indication of specific features of water exchange in the Black Sea. Oceanology 47 (3), 325—333, https://doi.org/10.1134/S0001437007.

Knyazev, V.Yu., Kossyi, I.A., Malykh, N.I., Yampolskii, E.S., 2003. Penetration of microwave radiation into water: Effect of induced transparency. Tech. Phys. 48, 1489—1492, https://doi.org/10.1134/1.1626786.

Kochanski, A., Koracin, D., Dorman, C.E., 2006. Comparison of wind-stress algorithms and their influence on wind-stress curl using buoy measurements over the shelf off Bodega Bay, California. Deep-Sea Res. Pt. 53 (25—26), 2865—2886, https://doi.org/10.1016/j.dsr2.2006.07.008.

Lee, Z-P., Darecki, M., Carder, K.L., Davis, C.O., Stramski, D., Rhea, W.J., 2005. Diffuse attenuation coefficient of downwelling irradiance: An evaluation of remote sensing methods. J. Geophys. Res.-Oceans. 110 (C02017), https://doi.org/10.1029/2004JC002573.

Li, X., Dong, C., Clemente-Colón, P., Pichel, W.G., Friedman, K.S., 2004. Synthetic aperture radar observation of the sea surface imprints of upstream atmospheric solitons generated by flow impeded by an island. J. Geophys. Res.-Oceans 109 (C2), C02016, https://doi.org/10.1029/2003JC002168.

Li, X., Zheng, W., Zou, C.-Z., Pichel, W.G., 2008. A SAR observation and numerical study on ocean surface imprints of atmospheric vortex streets. Sensors 8 (5), 3321—3334, https://doi.org/10.3390/s8053321.

Li, X., Zheng, W., Yang, X., Li, Z., Pichel, W.G., 2011. Sea surface imprints of coastal mountain lee waves imaged by synthetic aperture radar. J. Geophys. Res.-Oceans 116 (C2), C02014, https://doi.org/10.1029/2010JC006643.

Liu, A.Q., Moore, G.W.K., Tsuboki, K., Renfrew, I.A., 2004. A high-resolution simulation of convective roll clouds during a cold-air outbreak. Geophys. Res. Lett. 31 (3), https://doi.org/10.1029/2003gl018530.

Liu, S., Li, Z., Yang, X., Pichel, W., Yu, Y., Zheng, Q., Li, X., 2010. Atmospheric frontal gravity waves observed in satellite SAR images of the Bohai Sea and Huanghai Sea. Acta Oceanol. Sin. 29 (5), 35—43, https://doi.org/10.1007/s13131-010-0061-8.

Magalhaes, J.M., Araújo, I.B., da Silva, J.C.B., Grimshaw, R.H.J., Davis, D., Pineda, J., 2011. Atmospheric gravity waves in the Red Sea: a new hotspot. Nonlinear Proc. Geoph. 18, 71—79, https://doi.org/10.5194/npg-18-71-2011.

Malacic, V., Orlic, M., 1993. On the origin of the inverted-barometer effect at subinertial frequencies. Il Nuovo Cimento. Maggio-Glugno. 16 C (3), 265—288, https://doi.org/10.1007/BF02524229.

Monserrat, S., Vilibic, I., Rabinovich, A.B., 2006. Meteotsunamis: atmospherically induced destructive ocean waves in the tsunami frequency band. Nat. Hazard Earth Sys. 6 (6), 1035—1051, https://doi.org/10.5194/nhess-6-1035-2006.

Morel, A., Huot, Y., Gentili, B., Werdell, P.J., Hooker, S.B., Franz, B.A., 2007. Examining the consistency of products derived from various ocean color sensors in open ocean (Case 1) waters in the perspective of a multi-sensor approach. Remote Sens. Environ. 111 (1), 69—88, https://doi.org/10.1016/j.rse.2007.03.012.

Nappo, C.J., 2002. An introduction to atmospheric gravity waves. International Geophysics, Acad. Press, 276 pp.

Pegau, W.S., Gray, D., Zaneveld, J.R.V., 1997. Absorption and attenuation of visible and near-infrared light in water: dependence on temperature and salinity. Appl. Optics 36 (24), 6035—6046, https://doi.org/10.1364/AO.36.006035.

Phillips, O., 1977. The dynamics of the upper ocean (2nd edn.). Cambridge Univ. Press, 344 pp.

Plougonven, R., Zhang, F., 2014. Internal gravity waves from atmospheric jets and fronts. AGU. Rev. Geophys. 52 (1), 32—76, https://doi.org/10.1002/2012RG000419.

Rabinovich, A.B., 2008. Seiches and Harbour Oscillations. In: Kim, Y. (Ed.), Handbook of Coastal and Ocean Engineering World Scientific. California State Univ., Los Angeles, 193—236.

Sachsperger, J., Serafin, S., Grubi, V., Stiperskic, I., Pacid, A., 2018. The amplitude of lee waves on the boundary-layer inversion. Q. J. Roy. Meteor. Soc. 143 (702), 27—36, https://doi.org/10.1002/qj.2915.

Sheberstov, S.V., Lukyanova, E.A., 2007. A system for acquisition, processing and storage of satellite and field biooptical data. In: Proc. IV Int. Conf.: Current Problems in Optics of Natural Waters. Nizhny Novgorod, September 11—15, 179—183.

Suslin, V.V., Slabakova, V.R., Churilova, T.Y., 2017. Diffuse attenuation coefficient for downwelling irradiance at 490 nm and its

spectral characteristics in the Black Sea upper layer: modeling, in situ measurements and ocean color data. In: Proc. SPIE, 23rd International Symposium on Atmospheric and Ocean Optics: Atmospheric Physics, 10466, 104663H, https://doi.org/10.1117/12.2287367.

Vachon, P.W., Johannessen, O.M., Johannessen, J.A., 1994. An ERS 1 synthetic aperture radar image of atmospheric lee waves. J. Geophys. Res.-Oceans 99 (C11), 22483—22490, https://doi.org/10.1029/94JC01392.

Valenzuela, G.R., 1978. Theories for the interaction of electromagnetic and oceanic waves — a review. Bound.-Lay. Meteorol. 13, 61—85, https://doi.org/10.1007/BF00913863.

Wunsch, C., Stammer, D., 1997. Atmospheric loading and the oceanic "inverted barometer" effect. Rev. Geophys. 35 (1), 79—107, https://doi.org/10.1029/96RG03037.

Zheng, Q., Yan, X.-H., Klemas, V., Ho, C.-R., Kuo, N.-J., Wang, Z., 1998. Coastal lee waves on ERS-1 SAR images. J. Geophys. Res.-Oceans 103 (C4), 7979—7993, https://doi.org/10.1029/97JC02176.